Journal of Zhejiang University-SCIENCE A (Applied Physics & Engineering) in press
www.jzus.zju.edu.cn; www.springer.com/journal/11582
E-mail: jzus_a@zju.edu.cn

Research Article

https://doi.org/10.1631/jzus.A2400100

Analyzing the strengthening effect of steel-ultra high performance concrete composite on segmental linings

Renpeng CHEN[1,2,3], Meng FAN[1,2,3], Hongzhan CHENG[1,2,3]✉, Huaina WU[1,2,3], Yang ZHANG[4], Bingyong GAO[1,2,3], Shiqiang RUAN[1,2,3]

[1]*Research Center of Underground Space Advanced Technology, Hunan University, Changsha 410082, China*
[2]*Key Laboratory of Building Safety and Energy Efficiency of the Ministry of Education, Hunan University, Changsha 410082, China*
[3]*Department of Civil Engineering, Hunan University, Changsha 410082, China*
[4]*Key Laboratory for Wind and Bridge Engineering of Hunan Province, College of Civil Engineering, Hunan University, Changsha 410082, China*

Abstract: This study aims to assess the comprehensive strengthening effect of a steel-UHPC (ultra high performance concrete) composite strengthening method. The axial force-moment interaction curve (*N-M* curve) was calculated in a novel way, using cross-sectional strains at ultimate states as well as real-time stress measurements for each material. The enclosed area of the *N-M* curve was defined as a comprehensive performance index for the system. We validate our approach with comparisons to numerical modeling and full-scale four-point bending experiments. Additionally, strengthening effects were compared for different sagging and hogging moments based on material stress responses, and the impact of various strengthening parameters was analyzed. We find that the N-M curve of the strengthened cross-section envelops that of the un-strengthened cross-section. Notably, improvements in flexural capacity are greater under sagging moments during the large eccentric failure stage, and greater under hogging moments during the small eccentric failure stage. This discrepancy is attributed to the strength utilization of strengthening materials. These findings provide a reference for understanding the strengthening effects and parameters of steel-UHPC composite.

Key words: Strengthening effects; Steel-UHPC composite; Axial force-moment interaction curve; Shield segmental linings

1 Introduction

The development of underground space in urban environments has become crucial for tackling population density and traffic congestion issues (Liao et al., 2013; Chen et al., 2015; Liao et al., 2009, 2018). However, the required underground construction can pose risks to nearby existing shield tunnels (Cheng et al., 2020; Chen et al., 2020; Cheng et al., 2021), such as severe structural damage (Chang et al., 2001; Huang et al., 2017; Zhang et al., 2013; Li et al., 2018). Therefore, it is essential to develop strengthening methods that can safeguard such shield tunnels.

Various methods have been proposed to enhance the bearing capacity and stiffness of shield tunnels, including the conventional steel plate strengthening method and the FRP (fiber reinforced polymer) strengthening method (Huang et al., 2017; Huang and Zhang, 2016). The steel plate strengthening method utilizes rigid materials to improve stiffness and bearing capacity, but can also lead to interfacial damage and brittle failure (Liu et al., 2018). On the other hand, the FRP strengthening method employs flexible materials to enhance stiffness and resistance to cracking, but can cause limitations in bearing capacity (Zhang et al., 2023). Recently, the steel-UHPC composite strengthening method has been proposed (Chen et al., 2024). Using UHPC has shown promise in slowing crack propagation and improving synergistic load-bearing between the strengthening layer and damaged concrete structures (Qu et al., 2020; Zhu et al., 2021, 2020a; Zhang et al., 2019). Additionally, using UHPC reduces the required amount of steel, resulting in cost savings (Shao et al., 2021).

✉ Hongzhan CHENG, hzcheng@hnu.edu.cn

Received Feb. 26, 2024; Revision accepted June 24, 2024; Crosschecked

Full-scale experiments have demonstrated that the steel-UHPC composite strengthening method significantly enhances structural flexural capacity, stiffness, and ductility during failure (Ma, 2021; Chen et al., 2024). However, the number of test specimens in these studies has been limited, due to factors such as complex loading equipment, extended testing periods, and high costs. It is also important to note that the segmental linings in these recent experiments were only subjected to bending moments (Ma, 2021). In real scenarios, segmental linings will experience a combination of bending moments and axial forces, with the flexural capacity being heavily influenced by the axial force (Lee and Ge, 2001). Also, current tests and numerical simulations primarily focus on the structural mechanical response under a single axial force (Li et al., 2015a, 2015b). The strengthening effect is typically evaluated based on improvements in structural characteristic loads, such as cracking loads, yield loads, and ultimate loads (Zhang et al., 2019; Zhang et al., 2020). Furthermore, shield tunnels are subjected to various external disturbances, including vertical loading (Huang et al., 2017), vertical unloading (Meng et al., 2020), and lateral unloading (Cheng et al., 2020). Vertical loading leads to a significant increase in axial force, while vertical and lateral unloading cause decreases in axial force. As a result, the segmental lining may experience diverse combinations of axial forces and bending moments.

Therefore, a study of failure states which considers all internal forces is needed to understand the effectiveness of steel-UHPC composite strengthening methods. The *N-M* (axial force-moment interaction) curve is an essential tool for describing the flexural capacity of reinforced concrete structures across all axial force levels (Liu et al., 2023). Meanwhile, strengthened segment linings consist of different materials, each with distinct mechanical properties. Thus, real-time monitoring and assessment of the stress state of each material is critical to capture all possible failure states. However, few studies have addressed these issues.

With these issues in mind, we propose an analytical method to calculate the *N-M* response of segmental linings strengthened by steel-UHPC composite materials. Additionally, we develop a numerical model to validate this analytical solution. Subsequently, we investigate and compare the strengthening effects under sagging and hogging moments, and discuss the differing material stress responses. Finally, using *N-M* curves, we evaluate the mechanical performance of segmental linings with different strengthening parameters.

2 Analytical solution of the N-M curve

2.1 Basic assumption

We introduce a novel method to compute the *N-M* curve for segmental linings strengthened by steel-UHPC composites. The proposed method is based on the following assumptions:

a) The cross-section of the segmental lining follows the plane section assumption.

b) The interface between the strengthening layer and the segmental lining has sufficient connection strength.

c) Under sagging moments, the criteria for large and small eccentric failures are the yielding of tensile steel rebars and the collapse of the compressed concrete zone, respectively. Under hogging moments, the criteria for large and small eccentric failures are the yielding of tensile steel rebars and the failure of the compressed UHPC zone, respectively.

d) We use constitutive models of the materials as depicted in Fig. 1. The constitutive model for concrete is based on the work of Zhang et al. (2019), and is shown in Eq. (1).

$$\sigma_c=\begin{cases}0, & \text{if } \varepsilon_{t0}<\varepsilon_c\\ E_c\varepsilon_c, & \text{if } 0<\varepsilon_c<\varepsilon_{t0}\\ -f_c\left[2\dfrac{\varepsilon_c}{\varepsilon_{c0}}-\left(\dfrac{\varepsilon_c}{\varepsilon_{c0}}\right)^2\right], & \text{if } -\varepsilon_{c0}<\varepsilon_c<0\\ -f_c, & \text{if } \varepsilon_c<-\varepsilon_{c0}\end{cases} \tag{1}$$

Here, f_c and f_t denote the compressive and the tensile strength of concrete, respectively, ε_{c0} (= 0.002), ε_{cu} (= 0.0033), and ε_{t0} (= f_t/E_c) stand for the compression hardening strain, compression failure strain, and tensile cracking strain of concrete, respectively, and E_c denotes the Young's modulus of the concrete. Both the steel plate and steel rebars are considered perfect elastoplastic materials, and are described by **Eq. (2)**.

$$\sigma_s=\begin{cases}f_y, & \text{if } \varepsilon_y<\varepsilon_s\\ E_s\varepsilon_s, & \text{if } -\varepsilon_y<\varepsilon_s<\varepsilon_y\\ -f_y, & \text{if } \varepsilon_s<-\varepsilon_y\end{cases} \tag{2}$$

Here, f_y and ε_y denote the yield stress and the yield

strain of the steel plate and steel rebars, respectively; and E_s denotes the Young's modulus of the steel plate and steel rebars. The constitutive model for UHPC is based on the study by Zhang et al. (2020), and is provided in **Eq. (3)**.

$$\sigma_{\text{uhpc}}=\begin{cases} f_{\text{tuhpc}}, & \text{if } \varepsilon_{\text{tuhpc}} \le \varepsilon_{\text{uhpc}} \\ E_{\text{uhpc}}\varepsilon_{\text{uhpc}}, & \text{if } -\varepsilon_{\text{cuhpc0}} \le \varepsilon_{\text{uhpc}} < \varepsilon_{\text{tuhpc}} \\ -f_{\text{cuhpc}}, & \text{if } -\varepsilon_{\text{cuhpcu}} \le \varepsilon_{\text{uhpc}} < -\varepsilon_{\text{cuhpc0}} \end{cases} \tag{3}$$

Here, f_{cuhpc} and f_{tuhpc} denote the compressive and the tensile strength of UHPC, respectively, E_{uhpc} denotes the Young's modulus of the UHPC, $\varepsilon_{\text{uhpc0}}$ (= 0.0028), $\varepsilon_{\text{cuhpcu}}$ (= 0.0035), and $\varepsilon_{\text{tuhpc}}$ (= $f_{\text{tuhpc}}/E_{\text{uhpc}}$) stand for the compression hardening strain, compression failure strain, and tensile cracking strain of UHPC, respectively.

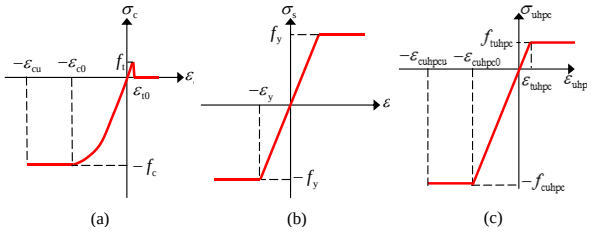

Fig. 1. The constitutive models used for (a) concrete; (b) steel; (c) UHPC.

2.2 Analytical model and calculation method

As shown in Fig. 2, the cross-section of the strengthened segmental lining comprises steel rebars, concrete, a steel plate, and UHPC. When only subjected to sagging moments, the strengthening layer is placed on the tensile side. Conversely, under just hogging moments, the strengthening layer operates in compression. Experimental studies on similar structures have shown that when exposed to solely sagging or hogging moments, tensile failure occurs (Ma, 2021). Specifically, the location of failure, whether in tension or compression, is primarily determined by the magnitude of the axial force. At low axial forces, the cross-section undergoes large eccentric failure, which is characterized by the failure of the tension zone. The yielding of steel rebars, which act as the final tensile-yielding material, governs this large eccentric failure under both sagging and hogging moments. On the other hand, at high axial forces, the cross-section experiences small eccentric failure, which is characterized by the failure of the compression zone. To determine the N-M curve, it is crucial to continuously calculate the failure state across all axial force levels. The strain state of the cross-section directly corresponds to its internal force. Therefore, by resolving the strain state from large eccentric failure to small eccentric failure, the flexural capacity can be determined at each time step.

In Fig. 2, the blue double-dashed lines represent the strain of the cross-section during the large eccentric failure stage, with the yield strain of the steel bar in the tension zone fixed at a critical value. As the axial force increases, the compression zone progresses towards the ultimate compressive strain of the concrete. A denser double-dashed line indicates a larger bending moment on the cross-section, as depicted by the blue arrow. The solid red line corresponds to the critical failure strain state, where the compression zone fails and the tension zone yields, indicating the simultaneous occurrence of large and small eccentric failures.

As the axial force continues to increase, the failure of the cross-section is primarily governed by damage to the compression zone. During the small eccentric failure stage, the ultimate compressive strains of concrete and UHPC serve as fixed points for sagging and hogging moments, respectively. As the axial force on the cross-section increases further, the steel rebars gradually transition from tension to compression, as depicted by the green dashed line. The dashed line becoming more sparse, as shown by the green arrow, indicates a weaker bending moment on the cross-section.

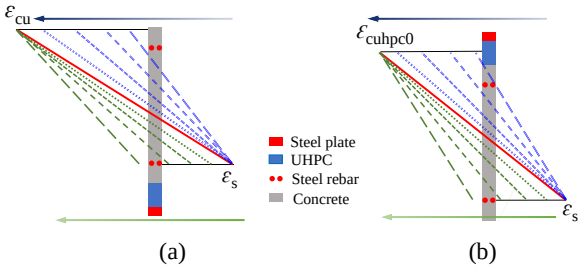

Fig. 2. The cross-sectional strain evolution process for (a) sagging moment; (b) hogging moment.

The process of determining the N-M curve is illustrated in Fig. 3. The calculation diagrams for the reinforced cross-section under pure sagging and hogging moments are shown in Figs. 4 and 5, respectively. Initially, the geometric and physical properties of the cross-section are set based on Figs. 4 and 5. The initial value of axial force is set to 0 kN. The critical characteristic strains for both large and small eccentric failures are known. The cross-section curvature (κ) is known from the assumed height of

the compression zone (h_c) and the characteristic strains corresponding to different eccentric failures. The stress of each material is then calculated using the height of the compression zone (h_c), the cross-section curvature (κ), and the constitutive equations. These stress expressions are then substituted into the axial force balance equation, and the axial force (N) is calculated using Eq. (4):

$$N = \int_A \delta(y)\mathrm{d}A \qquad (4)$$

where y represents the coordinate axis along the cross-section's height as depicted in Figs. 4 and 5. The general expressions for axial force (N) are given by Eqs. (S1) and (S3) in the supplementary material. A state coefficient of either 1 (stress) or 0 (no stress) is introduced to indicate whether each material is under stress. By utilizing Eq. (1), the compression zone height (h_c) is determined, along with the cross-section curvature (κ). The stress values for each material are then calculated and input to the bending moment balance equation, determining the flexural capacity, as given by Eq. (5):

$$M = \int_A \delta(y)y\mathrm{d}A \qquad (5)$$

The general expressions for bending moment (M) are provided in Eqs. (S2) and (S4) in the supplementary material. If the calculated bending moment is greater than zero, the stress state of each material is readjusted in real time for the subsequent cycle, based on a comparison between the calculated material strains and the characteristic strains from the constitutive relationship. The state coefficients are adjusted correspondingly according to Tables S1 and S2 in the supplementary material. Then, the axial force is increased by 1 kN for the next round of calculations. Regardless of whether the moment is sagging or hogging, the flexural capacity is always assigned a positive value. The calculation concludes when the calculated bending moment becomes negative.

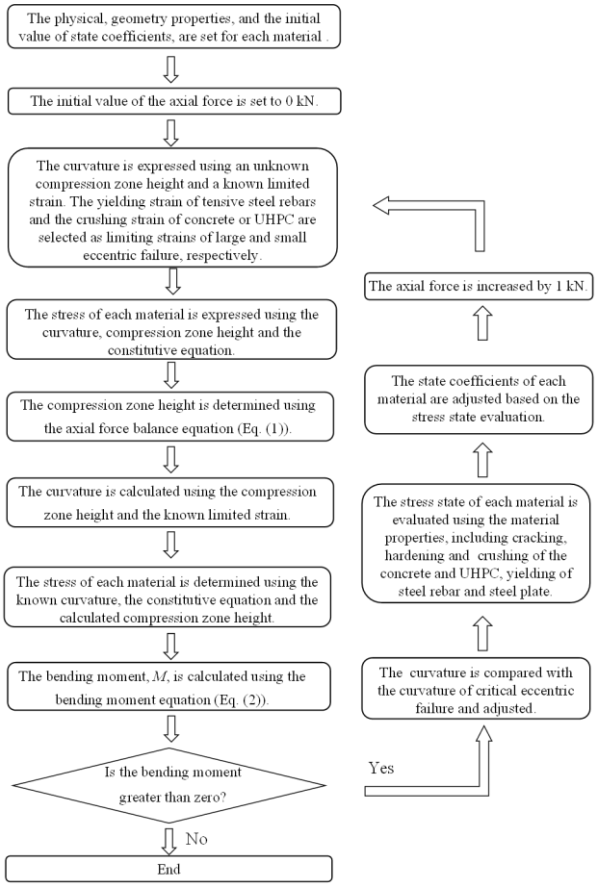

Fig. 3. *N-M* curve calculation flow chart for the steel-UHPC-strengthened segmental lining.

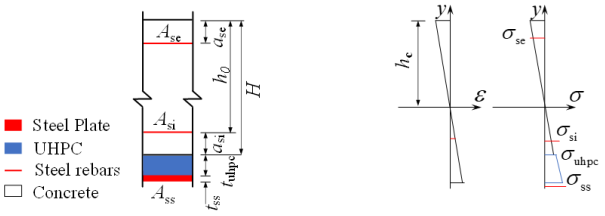

(a) (b)

Fig. 4. Calculation diagram for the strengthened cross-section under a sagging moment: (a) structural dimensional; (b) strain and stress distribution; A_{si}, A_{se}, and A_{ss} denote the area of the intrados steel rebars, extrados steel rebars, and steel plate layer, respectively; a_{se} and a_{si} denote the thickness of the inner and outer protective layer, respectively; t_{ss} and $t_{uhpc,}$ denote the thickness of the steel plate and UHPC layer, respectively; h_0, h_c, and H denote the height of the tensile rebars to the edge of the compression zone, the compression zone height, and segment lining thickness, respectively; σ_{si}, σ_{se}, σ_{uhpc}, and σ_{ss} denote the stress of the intrados steel rebars, extrados steel rebars, the UHPC layer, and the steel plate layer, re-

spectively.

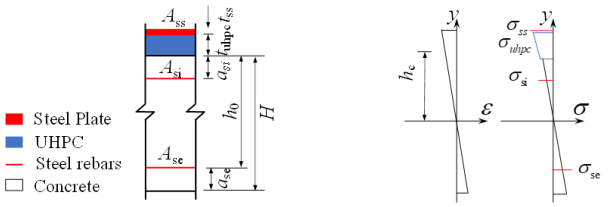

(a) (b)

Fig. 5. Calculation diagram for the strengthened cross-section under a hogging moment: (a) structural dimensional; (b) strain and stress distribution.

3 Validation with numerical and experimental results

3.1 Finite element model

The numerical model presented in Fig. 6a, which is a finite element model (FEM), reflects the dimensions of the segmental lining used in the full-scale experiments. It has an outer diameter of 6.2 m, an inner diameter of 5.5 m, a thickness of 0.35 m, a width of 1.5 m, and a central angle of 67.5° (Ma, 2021). For simplicity, the model does not consider the hand holes, as they have a negligible effect on the structural mechanical response. The UHPC and steel plates are sized to match the width of the segmental lining, and their thickness is determined based on experimental strengthening parameters, as illustrated in Fig. 6(b). The dimensions and positions of the anchor screws also align with the experimental design (Ma, 2021). To accurately simulate the behavior of the concrete, UHPC, steel plates, and anchor screws, solid elements (C3D8R) are utilized. The steel rebars are modeled using truss elements (T3D2). In total, the model is comprised of 17,630 elements.

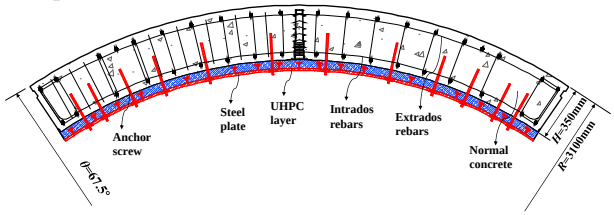

(a)

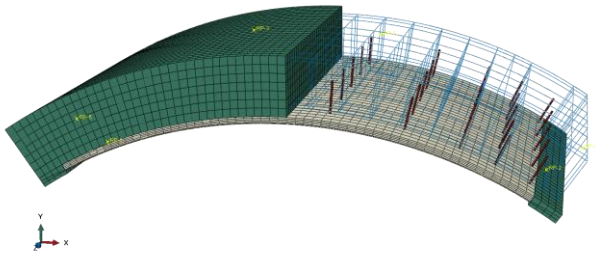

(b)

Fig. 6. The finite element model and its (a) geometric parameters; (b) numerical modelling cell structure.

3.2 Constitutive models and parameters

The damaged concrete plasticity model has been employed to represent the behavior and damage of both concrete and UHPC materials (Moradloo et al., 2019). Table 1 provides a list of the essential parameters required for this model. The parameters for C50 concrete are derived from the stress-strain curves obtained through uniaxial tensile and compressive tests (Mohourd and Gaqsiq, 2015). Similarly, the parameters for UHPC are determined from the uniaxial tensile and compressive tests conducted by Zhang et al. (2020), Yin et al. (2017), and Zhu et al. (2020b). The steel rebars are modeled using an ideal elastoplastic model (Samr and Sa, 2022), with the specific parameters provided in Table 2.

Table 1. Parameters of the plastic damage models for concrete and UHPC.

Parameters	Concrete	UHPC
Young's modulus E (GPa)	34.5	48.8
Poisson's ratio υ	0.2	0.15
Dilation angle (°)	38	15
Eccentricity ψ	0.1	0.1
Biaxial/uniaxial compression plastic strain ration f_{b0}/f_{c0}	1.16	1.16
Invariant stress ration K_c	0.67	0.67
Viscosity parameter μ	0.0003	0.0005

Table 2. Mechanical properties of the steel rebars and anchor screw.

Materials	Specification in Chinese	Young's modulus *E* (GPa)	Poisson's ratio υ	Yield stress f_y(MPa)
Steel rebar	HPB400	210	0.3	300
Steel rebar	HRB400	200	0.3	400
Steel plate	Q345	200	0.3	345
Anchor screw	12.9	200	0.3	1080

3.3 Constitutive models and parameters

As illustrated in Fig. 7a, the model's boundary condition is established as a simply supported beam with its two ends connected to supporting points "RP-1" and "RP-2" through the "coupling" function in Abaqus. These reference points are fixed in the Y-direction to prevent any movement. Additionally, the two side surfaces are fixed in the Z-direction to restrict rigid body motion. Fig. 7b illustrates the connection between the steel bar and the segment lining, which utilizes the "embedded" function. The interface between the segment lining and the UHPC employs cohesive and contact simulation, incorporating parameters obtained from the experiments conducted by Hussein et al. (2016), Semendary and Svecova (2020), and Zhu et al. (2020c). These parameters can be found in Table 3.

Experimental results indicate that the steel plate-UHPC interface (S-U interface) experiences significantly less stripping and slipping compared to the concrete-UHPC interface (C-U interface) (Ma, 2021). Consequently, we connect the steel plates to the UHPC using the "tie" function. Also, the anchor screws are embedded into the segment lining and the strengthening layer. The specimen is subjected to four-point loading, with a uniform distance of 0.8 m between the loading points, following the experimental setup in Ma (2021).

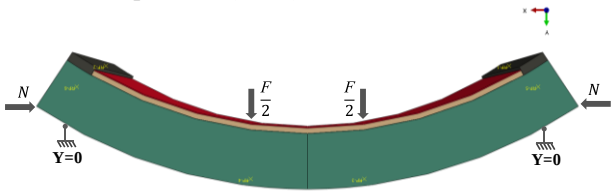

(a)

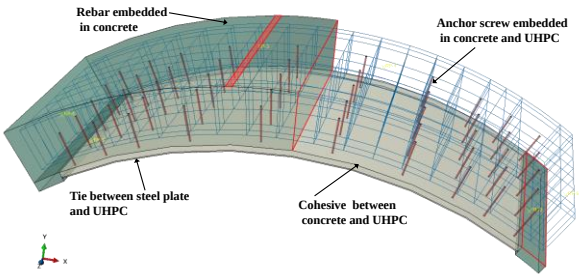

(b)

Fig. 7. Numerical model: (a) boundary condition; (b) interaction.

Table 3. Mechanical property parameters of the interface between the concrete and UHPC (Ma, 2021).

Parameters	Value
Normal stiffness component K_{nn} (N/mm^3)	1,358
Tangential stiffness component K_{ss}, K_{tt} (N/mm^3)	20,358
Interface contact stress τ_t^0 τ_n^0 τ_s^0 (MPa)	5.63
Total displacement (mm)	0.241
Viscosity index	0.001
Friction coefficient	1.44

3.4 Comparison between numerical and analytical results

In Table 4, we present the analytical solutions and numerical results for flexural capacity. The deviation between values ranges from -2.3% to 11.0%, which signifies the reliability of the proposed method. Fig. 8 shows a comparison between the FEM results and analytical solutions to illustrate the trends in flexural capacity. As depicted in Fig. 8a, increasing the steel plate thickness does not lead to a significant increase in the calculated flexural capacity. For example, the flexural capacity of case H-4-8 is 1.02 times that of case H-4-4 in both analytical solutions and FEM results. Moreover, Fig. 8b demonstrates that with a constant steel plate thickness, increasing the thickness of the strengthening layer improves the flexural capacity. In the analytical solution, the flexural capacity of case H-8-6 is 1.14 times that of case H-4-6, while in the FEM results, it is 1.18 times greater.

From Figs. 8c and d, it is evident that an increase in the axial force applied to both strengthened and un-strengthened segment linings results in a significant rise in flexural capacity. For the un-strengthened

cross-section, the flexural capacity of case H-0-0-N1100 exceeds that of case H-0-0-N000, by a factor of 1.56 in the FEM results and 1.71 in the analytical solutions. Similarly, for the strengthened cross-section, case H-4-6-N1100 exhibits higher flexural capacity compared to case H-4-6-N000, improving by factors of 1.50 in the FEM results and 1.40 in the analytical solutions. These comparisons demonstrate remarkable consistency between the FEM results and the theoretical calculations.

Under sagging moments, the flexural capacity of the numerical model is heavily influenced by interfacial failure (Ma, 2021). We conducted a comparison using the limited full-scale experimental data (Ma, 2021), with the results presented in Table 5. Increasing the steel plate thickness by 2 mm leads to a flexural capacity increase by a factor of 1.21 in experimental results, and 1.27 in the analytical solutions. Meanwhile, a 2 cm increase in UHPC thickness results in a bearing capacity increase of a factor of 1.13 in the experimental results, and 1.10 in the analytical solutions. Thus, both calculation methods effectively demonstrate the sensitivity of bearing performance to steel plate thickness. Moreover, the deviation between the calculations only ranges from -2.2% to 14.7%, confirming the reliability of our approach.

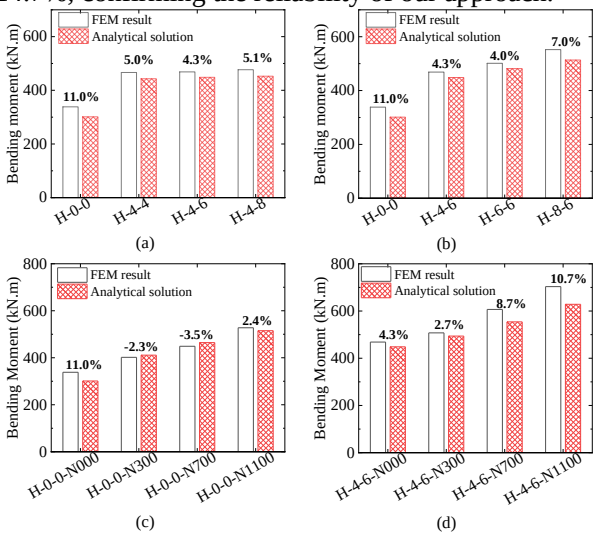

Fig. 8. Comparison of the analytical solutions and numerical results for: (a) steel plate thickness; (b) strengthening layer thickness; (c) axial force level of the un-strengthened structure; (d) axial force level of the strengthened structure.

Table 4. Comparison between numerical (FEM) results and analytical solutions under hogging moments.

Investigated variable	Figure	Cases number	FEM results (kN·m)	Analytical solution (kN·m)	Deviation
Steel plate thickness	Fig. 8(a)	H-0-0	338.3	301.0	11.0%
		H-4-4	466.3	443.0	5.0%
		H-4-6	468.6	448.5	4.3%
		H-4-8	476.7	452.5	5.1%
Strengthening layer thickness	Fig. 8(b)	H-0-0	338.3	301.0	11.0%
		H-4-6	468.6	448.5	4.3%
		H-6-6	501.3	481.4	4.0%
		H-8-6	552.0	513.3	7.0%
Axial force level of un-strengthened structure	Fig. 8(c)	H-0-0-N0	338.3	301.0	11.0%
		H-0-0-N300	401.9	410.9	-2.3%
		H-0-0-N700	448.9	464.4	-3.5%
		H-0-0-N1100	527.6	515.1	2.4%
Axial force level of strengthened structure	Fig. 8(d)	H-4-6-N0	468.6	448.5	4.3%
		H-4-6-N300	507.5	493.9	2.7%
		H-4-6-N700	606.8	554.1	8.7%
		H-4-6-N1100	703.4	628.5	10.7%

Note: The first letter in the case number indicates the type of load, where H and S signify hogging and sagging moments, respectively. The second number denotes the thickness of the strengthening layer, in centimeters. The third number represents the thickness of the steel plate, in millimeters. And the fourth number indicates the level of axial force, in kN. The deviation is calculated as the percent difference:

$$\text{Deviation}=\frac{\text{FEM result-Analytical solution}}{\text{FEM result}}\times 100\%$$

.

Table 5. Comparison between full-scale experimental results and analytical solutions under sagging moment.

Cases number	Full-scale experiment (kN·m)	Analytical solution (kN·m)	Deviation
S-0-0	466.5	398.2	14.7%
S-4-4	1204.4	1167.5	3.1%
S-4-6	1453.9	1485.6	-2.2%
S-6-6	1649.2	1626.8	1.4%

4 Validation with numerical and experimental results

4.1 Finite element model

4.1.1. Sagging moment

Fig. 9 shows the *N-M* curves for both strengthened and un-strengthened segmental linings under sagging moments. At zero axial force, the flexural capacities of the un-strengthened and strengthened segmental lining are 383.24 kN·m and 1485.60 kN·m,

respectively. Additionally, the *N-M* curves of both strengthened and un-strengthened segmental lining display consistent trends. During the tensile failure stage, i.e. large eccentric failure, the flexural capacity increases with increasing axial force. Conversely, during the compressive failure stage, i.e. small eccentric failure, the flexural capacity decreases with an increase in axial force. At the critical failure point, where compressive and tensile failure intersect, both the strengthened and un-strengthened structures exhibit their maximum flexural capacities, measuring 1888.97 kN·m and 1050.83 kN·m, respectively. Notably, large eccentric failure manifests as ductile failure due to the tensile yielding of steel rebars, while small eccentric failure is dominated by concrete crushing in the compression zone, which represents brittle failure. After strengthening, a reduction in the axial force corresponding to critical failure is observed, decreasing from 8600.00 kN to 5300.00 kN, as depicted in Fig. 9. This reduction lowers the likelihood of structural ductile failure. The enclosed area of the N-M curve is used as the compressive performance index, with a reference value of 1 for the un-strengthened segmental lining. The performance index of the strengthened cross-section is 2.04.

The increasing flexural capacity under sagging moments is shown in Fig. 10. After strengthening, a larger enhancement in flexural capacity is observed during the tensile failure stage. When the axial force is zero, the increase in flexural capacity reaches its maximum value of 1102.36 kN·m. Moreover, as the axial force increases, the increase in the flexural capacity gradually diminishes. Importantly, after reaching critical failure, the amplitude of the increase in flexural capacity rapidly decreases. The reason for this is discussed in Section 4.2.1.

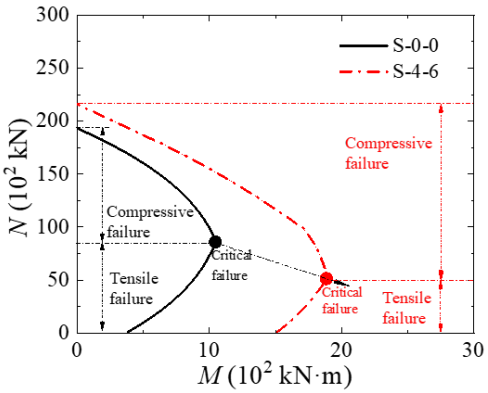

Fig. 9. *N-M* curves for strengthened and un-strengthened segment linings subjected to sagging moments.

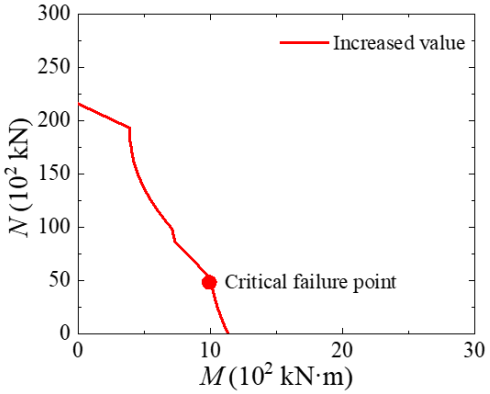

Fig. 10. The increased value of flexural capacity under sagging moments.

4.1.2. Hogging moment

Fig. 11 illustrates the *N-M* curves for strengthened and un-strengthened segmental linings subjected to hogging moments. When the axial force is zero, the flexural capacities of un-strengthened and strengthened segmental lining are 383.24 kN·m and 432.10 kN • m, respectively. Obviously, the improvement in flexural capacity is limited. At critical failure, both the strengthened and un-strengthened cross-section exhibit maximum flexural capacity, measuring 2413.58 kN·m and 1050.83 kN·m, respectively. Furthermore, strengthening the structure results in a significant increase in the axial force, corresponding to critical failure, as depicted in Fig. 11. This indicates a greater chance of ductile failure. The comprehensive performance index of the strengthened cross-section is 3.02. The compressive strength of UHPC, which is fully exerted under hogging moments, is superior to its tensile strength. This contributes to the higher comprehensive performance index.

We can observe the increased flexural capacity under hogging moments in Fig. 12. Unlike sagging moments, higher axial forces lead to greater increases in flexural capacity. Specifically, when the axial force is zero, the increase in flexural capacity is minimal, being 48.46 kN·m. Prior to critical failure, the improvement in flexural capacity increases with the increase in axial force. After critical failure, the rate of increase in flexural capacity slows as axial force increases, eventually displaying a gradual decrease. The reason for this phenomenon is discussed in Section 4.2.2.

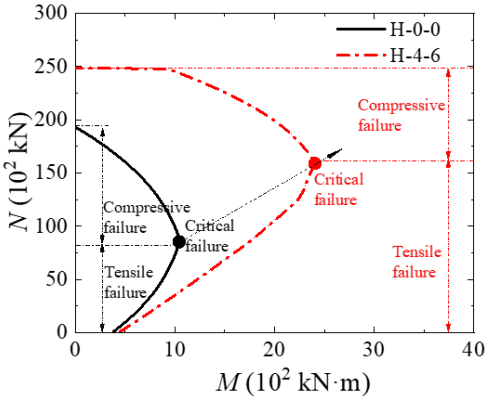

Fig. 11. *N-M* curves for strengthened and un-strengthened segment linings subjected to hogging moments.

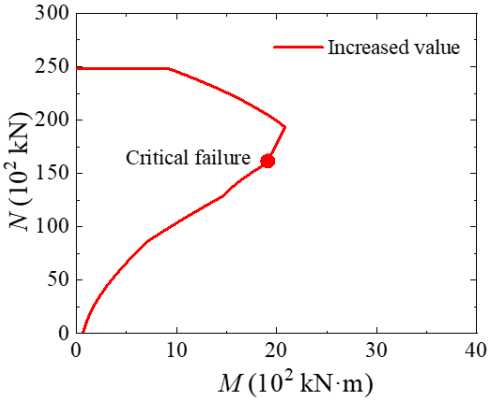

Fig. 12. Increased value of flexural capacity under hogging moments.

4.2 Material stress responses

4.2.1. Sagging moment

The strength utilization percentage, defined as the ratio between the stress and strength values of the bearing materials, is introduced to characterize the strengthening effect. Tension is considered positive, while compression is considered negative. Fig. 13 presents the strength utilization percentage of each material under sagging moments. During the large eccentric failure stage, as the axial force increases, the material response follows a sequence consisting of: compression hardening of extrados concrete, compression yielding of extrados steel rebars, then eventual collapse of extrados concrete. At zero axial force, the strength utilization percentage of the strengthening material is 100%, while that of the compressive concrete is -74.77%. The strengthening material that is in the tension zone governs the failure. The high material strength utilization explains the favorable strengthening effect during the tensile failure stage.

In the small eccentric failure stage, as the axial force increases, the material response follows a sequence of: the intrados steel bar no longer yielding under tension, the steel plate no longer yielding under tension, and then the UHPC no longer cracking. The utilization of tensile strength for the strengthening material gradually decreases, transitioning to a gradual increase in compressive strength utilization. For the case of full cross-section compression, both the steel plate and UHPC exhibit low ultimate strength utilizations of -28.68% and -22.85%, respectively. As a result, the increase in ultimate axial force is limited.

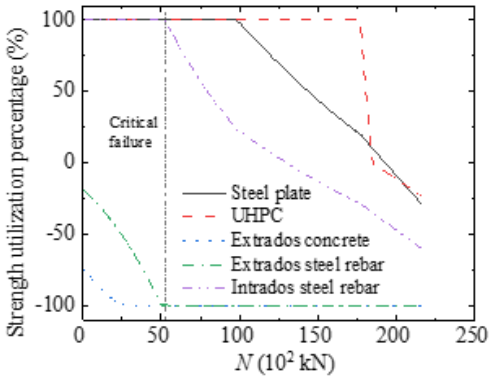

Fig. 13. Strength utilization percentage of each material under sagging moments.

4.2.2. Hogging moment

The strength utilization percentage of each material under hogging moments is illustrated in Fig. 14. During the large eccentric failure stage, as the axial force increases, the material response follows a sequence of: compression yielding of the steel plate, compression hardening of extrados concrete, and compression hardening of UHPC. At zero axial force, the strength utilizations of the steel plate and UHPC are notably low at -25.55% and -10.19%, respectively. This poor strengthening effect is attributed to the inadequate utilization of strengthening material in this scenario. However, as the axial force gradually increases, the strength utilization of the strengthening materials in the compression zone improves. This observation explains the sensitivity of the strengthening effect to axial force. Additionally, the high compressive strength of UHPC in the compression zone significantly enhances the corresponding axial force corresponding to critical failure.

In the small eccentric failure stage, as the axial force increases, the extrados steel bars transition from no longer yielding under tension, to a compression state. The utilization of tensile strength in the extrados

steel rebars gradually decreases, transitioning to a gradual increase in compressive strength utilization. Consequently, the rate of increase in flexural capacity decreases. The final compressive strength utilization of the extrados steel rebars is -35.93%.

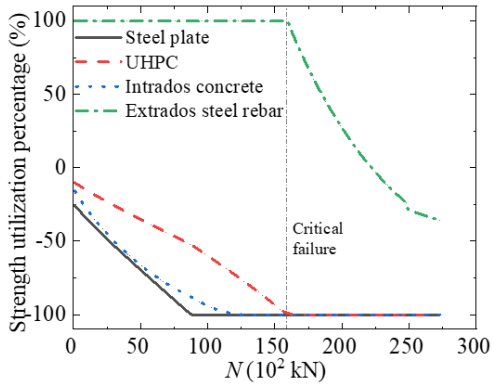

Fig. 14. Strength utilization percentage of each material under hogging moments.

4.3 Parameter analysis

4.3.1. Sagging moment

Fig. 15 depicts the *N-M* curves for segmental linings subjected to sagging moments, after being strengthened with varying thicknesses of steel plates and UHPC. In the large eccentric failure stage, increasing the thickness of the steel plate significantly enhances the flexural capacity compared to UHPC, primarily due to the superior tensile strength of steel. Specifically, when the axial force is zero, each 2 mm increase in steel plate thickness leads to a decrease in the increment of flexural capacity, from 304.58 kN·m to 248.97 kN·m. On the other hand, each 1 cm increase in UHPC thickness results in an increase in the increment of flexural capacity, ranging from 67.19 kN·m to 70.18 kN·m.

The axial force at critical failure decreases significantly as the steel plate thickness increases, as shown in Fig. 15a. For every 2 mm increase in steel plate thickness, the reduction in axial force at critical failure goes from 913.11 kN to 1201.33 kN. This indicates an increased risk of structural brittle failure. However, increasing the UHPC thickness mitigates this effect; with each 1 cm increase in UHPC thickness, the reduction in axial force at critical failure decreases from 212.25 kN to 101.63 kN, as shown in Fig. 15b. As the cross-section enters the small eccentric failure stage, the ultimate axial force becomes more sensitive to UHPC thickness.

Fig. 16 illustrates the rate of increase, as represented by the ratio between the comprehensive performance index of the strengthened structure and the un-strengthened structure. The ratio increases with the thickness of the strengthening materials. Specifically, with each 2 mm increment in steel plate thickness, the increase in this ratio gradually decreases from 0.18 to 0.09. On the other hand, for each 1 cm increase in UHPC thickness, the increase in the ratio rises from 0.15 to 0.17. Thus, increasing the thickness of UHPC provides greater benefit compared to increasing the steel plate thickness.

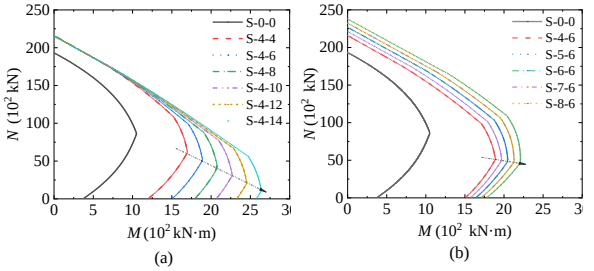

Fig. 15. N-M curves for segment linings subjected to sagging moments: (a) the effect of steel plate thickness; (b) the effect of UHPC thickness.

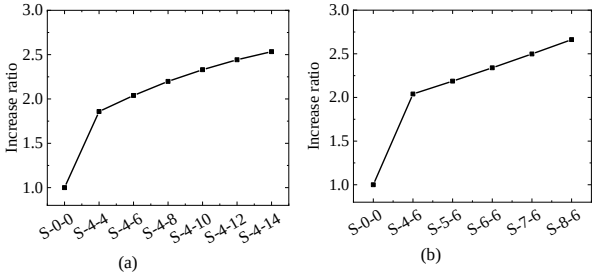

Fig. 16. The increase ratio of performance index of segment linings under sagging moments: (a) the effect of steel plate thickness; (b) the effect of UHPC thickness.

4.3.2. Hogging moment

We present *N-M* curves for segment linings strengthened with different thicknesses of steel plates and UHPC, under hogging moments, in Fig. 17. At low axial forces, the strengthening effect is insignificant regardless of the strengthening conditions. For example, when the axial force is zero, each 2 mm increase in steel plate thickness reduces the increment in flexural capacity from 5.44 kN·m to 1.43 kN·m. Conversely, with each 1 cm increase in UHPC thickness, the increment in flexural capacity increases from 16.65 kN·m to 21.04 kN·m. As the axial force gradually increases, the mechanical properties of the UHPC and steel plates begin to be leveraged, leading to a significant increase in flexural capacity. In-

creasing both the steel plate thickness and UHPC thickness enhances the axial force and flexural capacity at critical failure, as indicated by the dotted arrow in Fig. 17. With each 2 mm increase in steel plate thickness, the increment in axial force at critical failure decreases from 718.05 kN to 678.45 kN. Meanwhile, with each 1 cm increase in UHPC thickness, the increment in axial force at critical failure increases from 1651.40 kN to 1966.25 kN. Therefore, the benefit of increasing UHPC thickness is clear, as it significantly enhances the ultimate axial force.

Fig. 18 displays the strengthening increase ratio, i.e. the ratio between the performance index of the strengthened segment lining and that of the un-strengthened segment lining. As the thickness of the UHPC or steel plate increases, the performance index grows steadily. Specifically, with each 2 mm increment in steel plate thickness, the increase in the ratio remains stable around 0.23 to 0.24. On the other hand, for each 1 cm increase in UHPC thickness, the increase in the performance index rises from 0.70 to 0.89. Notably, increasing UHPC thickness more effectively enhances the performance index than increasing the steel plate thickness. This can be attributed to the full utilization of the strong compression performance characteristics of UHPC when in the compression region. Moreover, the thickness of UHPC is increased in centimeters, whereas the thickness of steel plate is increased in millimeters.

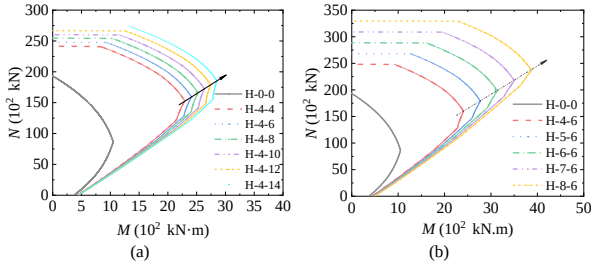

Fig. 17. N-M curves for segment linings under hogging moments: (a) the effect of steel plate thickness; (b) the effect of UHPC thickness.

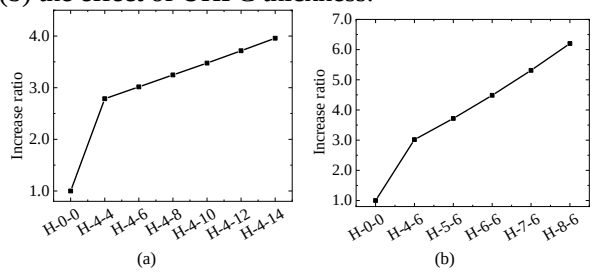

Fig. 18. Increase ratio of performance index of segment linings under hogging moments: (a) the effect of steel plate thickness; (b) the effect of UHPC thickness.

5 Conclusions

We presented a novel method for calculating the *N-M* curves of segmental linings strengthened by steel-UHPC composites, which was validated through comparisons with numerical modeling and full-scale bending experiments. The strengthening effects under both sagging and hogging moments were compared, and parameter analysis was conducted to examine the impact of different strengthening parameters.

The *N-M* curve calculation method was based on the cross-sectional strain at all ultimate states. The maximum calculation error between the analytical value and numerical value was less than 15%. Moreover, the analytical results were consistent with the numerical results across various strengthening parameters.

The disparity in strengthening effects under sagging and hogging moments primarily arose from the varying axial force thresholds required for the strength utilization of the steel-UHPC composite. Under sagging moments, in the large eccentric failure stage, the strengthening layer on the tensile side was fully utilized, resulting in a significant strengthening effect. In contrast under hogging moments, the strengthening effect requires a sufficient level of axial force to ensure further utilization of strengthening material in the compressive zone.

Changes in steel plate and UHPC thicknesses cause different strengthening effects and axial force values at critical failure. Under sagging moments, the flexural capacity at the large eccentric failure stage shows high sensitivity to steel plate thickness. However, this is accompanied by a significant decrease in the axial force at critical failure, indicating increased risk of brittle failure. Under hogging moments, increasing the UHPC thickness proves to be more effective at enhancing flexural capacity. Importantly, the axial force at critical failure also increases.

Steel plate and UHPC thicknesses also have distinct impacts on the comprehensive performance index. For every 2 mm increment in steel plate thickness, the increase in the performance index decreases from 0.18 to 0.09 under sagging moments,

while it remains between 0.23 and 0.24 under hogging moments. Additionally, a 1 cm increase in UHPC thickness results in a performance index improvement increase from 0.15 to 0.17 under sagging moments, and from 0.70 to 0.89 under hogging moments. This discrepancy arises from the exceptional compression properties of UHPC, which can be further leveraged in the compression zone.

Author contributions

Renpeng CHEN designed the research. Meng FAN, Bingyong GAO and Shiqiang RUAN processed the corresponding data. Meng FAN wrote the first draft of the manuscript. Huaina WU and Yang ZHANG helped to organize the manuscript. Hongzhan CHENG revised and edited the final version.

Conflict of interest

Renpeng CHEN, Meng FAN, Hongzhan CHENG, Huaina WU, Yang ZHANG, Bingyong GAO, Shiqiang RUAN declare that they have no conflict of interest.

References

Chang CT, Wang MJ, Chang CT, et al., 2001. Repair of displaced shield tunnel of the Taipei rapid transit system. Tunn Undergr Space Technol; 16:167–73. https://doi.org/10/dwbx79.

Chen RP, Chen S, Wu HN, et al., 2020. Investigation on deformation behavior and failure mechanism of a segmental ring in shield tunnels based on elaborate numerical simulation. Eng Fail Anal; 117:104960. https://doi.org/10.1016/j.engfailanal.2020.104960.

Chen RP, Gao BY, Ruan SQ, et al., 2024. Experimental study on the mechanical behavior of segmental joints of shield tunnels strengthened by a steel plate-UHPC composite. Tunnelling and Underground Space Technology. 144, 105536. https://doi.org/10.1016/j.tust.2023.105536

Chen RP, Tang LJ, Yin XS, et al., 2015. An improved 3D wedge-prism model for the face stability analysis of the shield tunnel in cohesionless soils. Acta Geotech; 10:683–92. https://doi.org/10.1007/s11440-014-0304-5.

Cheng HZ, Chen RP, Wu HN, et al., 2020. A simplified method for estimating the longitudinal and circumferential behaviors of the shield-driven tunnel adjacent to a braced excavation. Comput Geotech; 123:103595. https://doi.org/10.1016/j.compgeo.2020.103595.

Cheng HZ, Chen RP, Wu HN, et al., 2021. General solutions for the longitudinal deformation of shield tunnels with multiple discontinuities in strata. Tunn Undergr Space Technol; 107:103652. https://doi.org/10.1016/j.tust.2020.103652.

Huang HW, Shao H, Zhang DM, et al., 2017. Deformational responses of operated shield tunnel to extreme surcharge: a case study. Struct Infrastruct Eng; 13:345–60. https://doi.org/10.1080/15732479.2016.1170156.

Huang HW, Zhang DM, 2016. Resilience analysis of shield tunnel lining under extreme surcharge: Characterization and field application. Tunn Undergr Space Technol; 51:301–12. https://doi.org/10/f76hc5.

Hussein HH, Walsh KK, Sargand SM, et al., 2016. Interfacial Properties of Ultrahigh-Performance Concrete and High-Strength Concrete Bridge Connections. J Mater Civ Eng; 28:04015208. https://doi.org/10.1061/(ASCE)MT.1943-5533.0001456.

Lee KM, Ge XW, 2001. The equivalence of a jointed shield-driven tunnel lining to a continuous ring structure. Can Geotech J; 38:461–83.

Li MG, Chen JJ, Wang JH, et al., 2018. Comparative study of construction methods for deep excavations above shield tunnels. Tunn Undergr Space Technol; 71:329–39. https://doi.org/10.1016/j.tust.2017.09.014.

Li XJ, Yan ZG, Wang Z, et al., 2015. A progressive model to simulate the full mechanical behavior of concrete segmental lining longitudinal joints. Eng Struct; 93:97–113. https://doi.org/10.1016/j.engstruct.2015.03.011.

Li XJ, Yan ZG, Wang Z, et al., 2015. Experimental and analytical study on longitudinal joint opening of concrete segmental lining. Tunn Undergr Space Technol; 46:52–63. https://doi.org/10.1016/j.tust.2014.11.002.

Liao SM, Fan YY, Shi ZH, et al., 2013. Optimization study on the reconstruction and expansion of an underground rail transit center in Shanghai soft ground. Tunn Undergr Space Technol; 38:435–46. https://doi.org/10.1016/j.tust.2013.08.001.

Liao SM, Cheng CH, Chen LS, 2018. The planning and construction of a large underpass crossing urban expressway in Shanghai: An exemplary solution to the traffic congestions at dead end roads. Tunn Undergr Space Technol; 81:367–81. https://doi.org/10.1016/j.tust.2018.07.010.

Liao SM, Liu JH, Wang RL, et al., 2009. Shield tunneling and environment protection in Shanghai soft ground. Tunn Undergr Space Technol; 24:454–65. https://doi.org/10.1016/j.tust.2008.12.005.

Liu DJ, Zhang Y, Zuo JP., 2023. Strengtheing evaluation and evolution law of the bearing capacity of the normal section of the shield tunnel based on N-M curve. J China Univ Min Technol; 52:76–85.

Liu X, Jiang ZJ, Yuan Y, et al., 2018. Experimental investigation of the ultimate bearing capacity of deformed segmental tunnel linings strengthened by epoxy-bonded steel plates. Struct Infrastruct Eng; 14:685–700. https://doi.org/10.1080/15732479.2017.1354892.

Ma QL, 2021. Research on Mechanical Properties of Shield Tunnel Segments Strengthened by Ultra-High Performance Concrete. Hunan University.

Meng FY, Chen RP, Wu HN, et al., 2020. Observed behaviors of a long and deep excavation and collinear underlying tunnels in Shenzhen granite residual soil. Tunn Undergr Space Technol; 103:103504. https://doi.org/10.1016/j.tust.2020.103504.

MOHURD (Ministry of Housing and Urban-Rural Developmentof the People's Republic of China), GAQSIQ

(General Administration of Quality Supervision, Inspection and Quarantine of the People's Republic of China), 2015. Chinese Code for Design of Concrete Structured, GB 50010–2010, National Standards of the People's Republic of China (in Chinese).

Moradloo AJ, Adib A, Pirooznia A, 2019. Damage analysis of arch concrete dams subjected to underwater explosion. Appl Math Model; 75:709–34. https://doi.org/10.1016/j.apm.2019.04.064.

Qu SQ, Zhang Y, Zhu YP, et al., 2020. Prediction of tensile response of UHPC with aligned and ZnPh treated steel fibers based on a spatial stochastic process. Cem Concr Res; 136:106165. https://doi.org/10.1016/j.cemconres.2020.106165.

SAMR (State Administration for Market Regulation), SA (Standardization Administration of the People's Republic of China), 2022. Test Methods of Steel for Reinforcement of Concrete, GB/T 28900–2022, National Standards of the People's Republic of China (in Chinese).

Semendary AA, Svecova D, 2020. Interfacial Parameters for Bridge Connections at High-Strength Concrete–Ultrahigh-Performance Concrete Interface. J Mater Civ Eng; 32:04020060. https://doi.org/10.1061/(ASCE)MT.1943-5533.0003107.

Shao XD, He GD, Shen XJ, et al., 2021. Conceptual design of 1000 m scale steel-UHPFRC composite truss arch bridge. Eng Struct; 226:111430. https://doi.org/10.1016/j.engstruct.2020.111430.

Shao XD, Yi DT, Huang ZY, et al., 2013. Basic Performance of the Composite Deck System Composed of Orthotropic Steel Deck and Ultrathin RPC Layer. J Bridge Eng; 18:417–28. https://doi.org/10.1061/(ASCE)BE.1943-5592.0000348.

Shao XD, Zeng HQ, Cao JH, 2023. Flexural behavior of fully prefabricated large-cantilevered high strength steel-UHPC composite bent caps. J Constr Steel Res; 204:107856. https://doi.org/10.1016/j.jcsr.2023.107856.

Yin H, Teo W, Shirai K, 2017. Experimental investigation on the behaviour of reinforced concrete slabs strengthened with ultra-high performance concrete. Constr Build Mater; 155:463–74. https://doi.org/10.1016/j.conbuildmat.2017.08.077.

Zhang JF, Chen JJ, Wang JH, et al., 2013. Prediction of tunnel displacement induced by adjacent excavation in soft soil. Tunn Undergr Space Technol; 36:24–33. https://doi.org/10.1016/j.tust.2013.01.011.

Zhang JL, Liu X, Ren TY, et al., 2019. Structural behavior of reinforced concrete segments of tunnel linings strengthened by a steel-concrete composite. Compos Part B Eng; 178:107444. https://doi.org/10/dz37.

Zhang, X, Lin, Z, Zhang, K, et al., 2023. Full–scale experimental test for load–bearing behavior of the carbon fiber shell reinforced stagger–jointed shield tunnel. Compos. Struct. 311, 116773. https://doi.org/10.1016/j.compstruct.2023.116773

Zhang Y, Li XL, Zhu YP, et al., 2020. Experimental study on flexural behavior of damaged reinforced concrete (RC) beam strengthened by toughness-improved ultra-high performance concrete (UHPC) layer. Compos Part B Eng;186:107834. https://doi.org/10.1016/j.compositesb.2020.107834.

Zhang Y, Zhu YP, Yeseta M, et al., 2019. Flexural behaviors and capacity prediction on damaged reinforcement concrete (RC) bridge deck strengthened by ultra-high performance concrete (UHPC) layer. Constr Build Mater;215:347–59. https://doi.org/10.1016/j.conbuildmat.2019.04.229

Zhu YP, Hussein HS, Kumar A, et al., 2021. A review: Material and structural properties of UHPC at elevated temperatures or fire conditions. Cem Concr Compos; 123:104212. https://doi.org/10.1016/j.cemconcomp.2021.104212.

Zhu YP, Zhang Y, Hussein HH, et al., 2020a. Flexural strengthening of reinforced concrete beams or slabs using ultra-high performance concrete (UHPC): A state of the art review. Eng Struct; 205:110035. https://doi.org/10.1016/j.engstruct.2019.110035.

Zhu YP, Zhang Y, Hussein HH, et al., 2020b. Numerical modeling for damaged reinforced concrete slab strengthened by ultra-high performance concrete (UHPC) layer. Eng Struct; 209:110031. https://doi.org/10.1016/j.engstruct.2019.110031.

Electronic supplementary materials

Tables S1-S2, Eqs. (S1)–(S4)

中文概要

题　目:钢-超高性能混凝土复合结构对盾构管片衬砌加固效果的分析

作　者: 陈仁朋[1,2,3]，凡猛[1,2,3]，程红战[1,2,3]，吴怀娜[1,2,3]，张阳[4]，阮世强[1,2,3]，高斌勇[1,2,3]

机　构: [1]湖南大学地下空间先进技术研究中心，中国长沙，410082；湖南大学建筑安全与节能教育部重点实验室，[2]中国长沙，410082；[3]湖南大学土木工程系，中国长沙，410082；[4]湖南省风工程与桥梁工程重点实验室，中国长沙，410082

目　的: 本研究旨在评估钢-超高性能混凝土（UHPC）复合加固方法的综合加固效果。

创新点: 该研究通过一种新颖的方法计算轴力-弯矩相互作用曲线（N-M 曲线），该方法利用极限状态下的截面应变以及各材料的实时应力测量。。

方　法: 1. 计算 N-M 曲线，使用截面应变和实时应力测量；2. 通过数值模拟和足尺四点弯曲实验验证计算方法；3. 基于材料应力响应比较不同正和负弯矩

的加固效果；3.分析各种加固参数的影响。

结　论： 1. 加固截面的 *N-M* 曲线包络了未加固截面的 *N-M* 曲线；2. 在正弯矩作用下，大偏心破坏阶段的抗弯能力提高更大，在负弯矩作用下，小偏心破坏阶段的抗弯能力提高更大；3. 加固效果的差异来自于加固材料利用率对轴力水准的阈值不同；4. 研究结果为理解钢-UHPC 复合材料的加固效果和参数提供了参考。

关键词： 加固效果；钢-UHPC 组合结构；轴力弯矩相互作用曲线；盾构管片衬砌